

Compressive sensing of frequency-dependent seismic radiation from subduction zone megathrust ruptures

Huajian Yao^{a,b,1}, Peter M. Shearer^b, and Peter Gerstoft^b

^aLaboratory of Seismology and Physics of Earth's Interior, School of Earth and Space Sciences, University of Science and Technology of China, Hefei, Anhui 230026, China; and ^bScripps Institution of Oceanography, University of California at San Diego, La Jolla, CA 92093

Edited by Barbara A. Romanowicz, University of California, Berkeley, CA, and approved February 4, 2013 (received for review July 25, 2012)

Megathrust earthquakes rupture a broad zone of the subducting plate interface in both along-strike and along-dip directions. The along-dip rupture characteristics of megathrust events, e.g., their slip and energy radiation distribution, reflect depth-varying frictional properties of the slab interface. Here, we report high-resolution frequency-dependent seismic radiation of the four largest megathrust earthquakes in the past 10 y using a compressive-sensing (sparse source recovery) technique, resolving generally low-frequency radiation closer to the trench at shallower depths and high-frequency radiation farther from the trench at greater depths. Together with coseismic slip models and early aftershock locations, our results suggest depth-varying frictional properties at the subducting plate interfaces. The shallower portion of the slab interface (above ~15 km) is frictionally stable or conditionally stable and is the source region for tsunami earthquakes with large coseismic slip, deficient high-frequency radiation, and few early aftershocks. The slab interface at intermediate depths (~15–35 km) is the main unstable seismogenic zone for the nucleation of megathrust quakes, typically with large coseismic slip, abundant early aftershocks, and intermediate- to high-frequency radiation. The deeper portion of the slab interface (~35–45 km) is seismically unstable, however with small coseismic slip, dominant high-frequency radiation, and relatively fewer aftershocks.

subduction zone earthquake | coseismic radiation and slip | aftershock distribution | depth-varying friction

Most great earthquakes [moment magnitude (M_w) >8.0] occur at the shallow plate interface between the subducting and overriding plates in subduction zones (1). Variations in the geometrical and physical properties of subducting interfaces and differences in composition and ambient tectonic environments of subduction zones (2, 3) lead to substantial variability in the rupture processes of megathrust earthquakes (1, 4, 5). The along-strike variations in rupture of these events are probably caused by variations in the distribution of asperities on the fault plane (1), as manifested by heterogeneous slip and rupture velocity on the fault planes in seismic and/or geodetic slip inversions (6–10) and complex patterns of high-frequency (HF) seismic radiation from waveform backprojection (11–19). The along-dip (or depth-dependent) rupture of megathrust earthquakes is typically harder to resolve seismically compared with along-strike rupture variations, because these giant events generally rupture further in the along-strike direction (6–10). However, depth-dependent frictional properties and stability regimes of subducting plate interfaces (20) imply along-dip variations of rupture behavior should occur. It is well known that shallower earthquakes in subduction zones, in particular tsunami earthquakes, have significantly longer source durations and depleted short-period energy (5, 21, 22). This is consistent with slower rupture propagation of tsunami earthquakes caused by soft low-rigidity sediments on the shallow plate interface (5, 22) and possibly the increase of dynamic pore pressure in the shallow up-dip region (23).

However, a detailed picture of depth-varying rupture processes of megathrust events (see Fig. 1 for a summary) was not well established until recently, from extensive seismological investigations of the 2011 M_w 9.0 Tohoku earthquake in Japan. This

earthquake exhibits apparent along-dip variations in rupture properties, with major slip occurring in the up-dip region closer to the trench as seen in finite-fault slip inversions (9, 10, 15), whereas HF radiation dominates in the down-dip region closer to the Japan coast as imaged using waveform backprojection (10, 14–18). Similarly, apparent along-dip rupture differences were observed for several other large megathrust events by comparing the slip distribution with HF radiation observations (4, 15). Because waveform backprojection usually uses velocity seismograms (i.e., proportional to the slip acceleration in the source region), observed backprojection power cannot be directly related to finite-fault slip models. Recently, comparisons between time-domain backprojection power at various frequency bands for the Tohoku earthquake (14, 16, 17) and the 2010 Maule earthquake in Chile (19) have also revealed frequency-dependent along-dip energy radiation, with higher-frequency radiation at deeper depths. However, due to poor spatial resolution of waveform backprojection at lower frequencies (17), there are large uncertainties in this type of comparison and the resulting inferences on the details of along-dip rupture characteristics.

We use compressive sensing (CS) (24–28) and seismic array data (Figs. S1 and S2) to systematically analyze the along-dip energy radiation at 0.06–0.6 Hz from the four largest megathrust earthquakes in the past 10 y (see *Materials and Methods*), i.e., the 2011 M_w 9.0 Tohoku earthquake in Japan, the 2010 M_w 8.8 Maule earthquake in Chile, the 2005 M_w 8.6 Sumatra earthquake, and the 2004 M_w 9.2 Sumatra earthquake. CS is a sparse-source inversion method with higher resolution than the conventional beamforming approach (29) or superresolution beamforming methods [e.g., multiple signal classification (MUSIC); refs. 30 and 31] in resolving two or multiple sources, in particular for transient earthquake signals. We compare the frequency-dependent energy radiation to the spatial distribution of major coseismic slip and the early aftershocks to infer the depth-varying frictional properties of subduction zone slab interfaces.

Results

The resulting spatiotemporal distributions of energy radiation at three representative frequencies for the four events (Figs. 2 and 3) show clear along-dip patterns, with low-frequency (LF) energy radiation much closer to the plate boundary near the trench. This feature is even more evident when we compare the along-dip average radiated power at various frequencies (Fig. 4) or over different frequency bands (Fig. 5). Because we use teleseismic data with nearly vertical rays leaving the source region, we do not have

Author contributions: H.Y., P.M.S., and P.G. designed research; H.Y. performed research; H.Y., P.M.S., and P.G. contributed new reagents/analytic tools; H.Y. analyzed data; and H.Y., P.M.S., and P.G. wrote the paper.

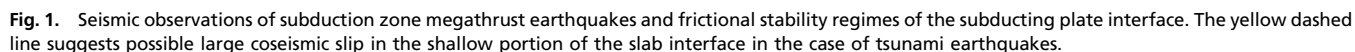
The authors declare no conflict of interest.

This article is a PNAS Direct Submission.

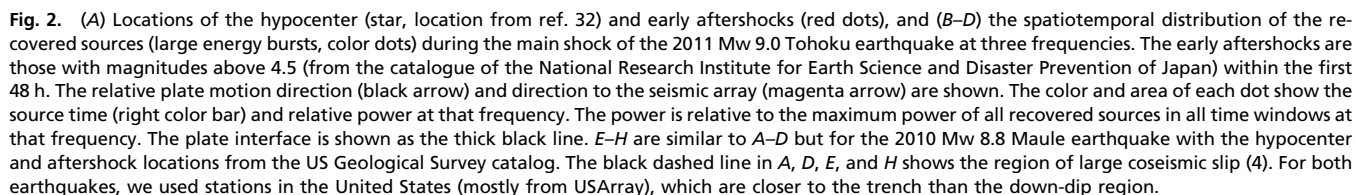
Freely available online through the PNAS open access option.

¹To whom correspondence should be addressed. E-mail: hjyao@ustc.edu.cn.

This article contains supporting information online at www.pnas.org/lookup/suppl/doi:10.1073/pnas.1212790110/-DCSupplemental.



an up-dip pattern closer to the trench for frequencies below 0.16 Hz (Figs. 2*D*, 4*A*, and 5*A*). This apparent along-dip shift of energy radiation is also evident in previous studies (14, 16, 17, 24), although detailed features may vary due to differences in methods or frequency bands. For the Maule earthquake, the general rupture behavior seen in the HF radiation at 0.48 Hz (Fig. 2*F*) is similar to that of previous backprojection studies (13, 17, 19). There is no clear migration pattern of seismic radiation above 0.1 Hz (Figs. 4*B* and 5*B*). However, at the low frequency of 0.08 Hz (Fig. 2*H*), the seismic radiation is much closer to the trench and there is little down-dip energy radiation, consistent with recent backprojection results (19). For the 2005 Sumatra



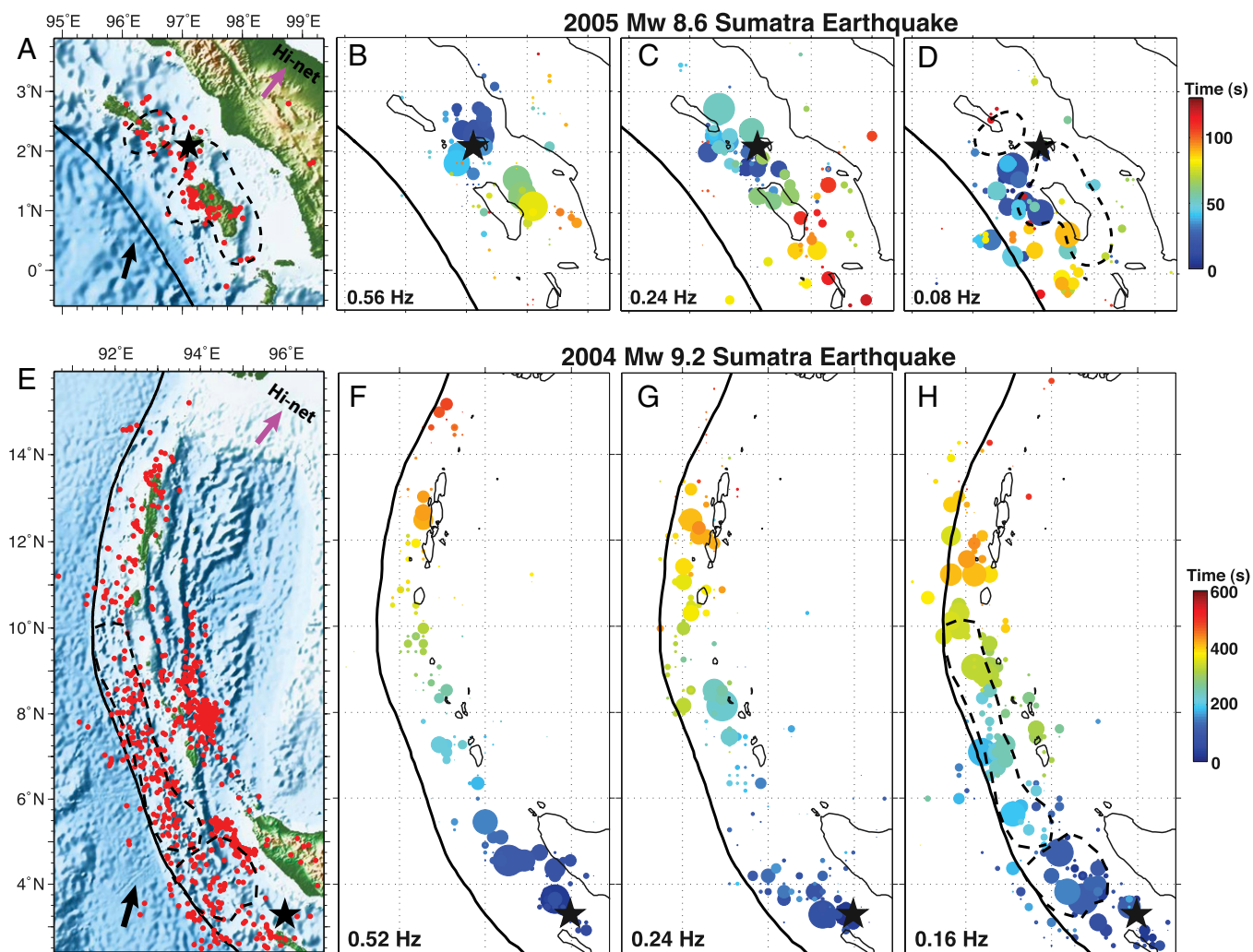


Fig. 3. Similar to Fig. 2 but for the 2005 Mw 8.6 Sumatra earthquake (A–D) and 2004 Mw 9.2 Sumatra earthquake (E–H). For both earthquakes, we used stations from the Hi-net array in Japan, which are closer to the down-dip region than the trench.

earthquake, the imaged HF radiation (Fig. 3B) is similar in location to that seen previously using backprojection (12). The mainshock radiation shows clear along-dip frequency-dependent characteristics (Figs. 3B–D, 4C, and 5C) with LF radiation systematically shallower (closer to the trench) than HF radiation. For the 2004 Sumatra event, the northward rupture is evident from the spatiotemporal distribution of energy radiation (Fig. 3F–H), consistent with previous backprojection results (11). The frequency- and depth-dependent seismic radiation of this event is obvious at intermediate to lower frequencies below 0.3 Hz (Figs. 4D and 5D). Above 0.3 Hz, the overall peak energy radiation mostly occurs at a similar distance to the trench (Fig. 4D).

Discussion and Summary

The systematic frequency/depth-varying seismic radiation pattern is not likely an imaging or depth-phase (18) artifact because the four events are analyzed using two different source-array geometries (Figs. 2A and E, and 3A and E), and backprojection of a number of moderate magnitude aftershocks has suggested no systematic bias that could cause HF energy to occur down-dip (4, 19). Therefore, the along-dip frequency-dependent seismic radiation characteristics for these earthquakes are real and imply variations of rupture processes and related changes in physical properties at the plate interface.

Not only does the seismic radiation of these megathrust earthquakes exhibit frequency/depth-varying properties, the coseismic slip and the distribution of early aftershocks also show some depth-varying features. The coseismic slip is not significant in the down-dip region for the Tohoku, Maule, and 2004 Sumatra earthquakes, where intermediate- to high-frequency radiation dominates. For the 2005 Sumatra earthquake, perhaps due to its smaller magnitude (Mw ~8.6), the large slip region correlates more with intermediate- to low-frequency radiation (Figs. 3C and D and 5C). The major coseismic slip mainly occurred in the up-dip region or around the hypocenter depths (Figs. 2A and E, 3A and E, and 5), in particular for the Tohoku earthquake and the 2004 Sumatra earthquake, for which large slip patches probably extend all of the way up-dip close to the trench (6, 9, 33). The large slip area corresponds well to the region where the intermediate- to low-frequency seismic radiation occurs (Figs. 2D and H, 3D and H, and 5). This implies that these megathrust earthquakes rupture more slowly and continuously in a large area in the up-dip region to generate LF seismic radiation along the shallower portion of the subduction plate interface. The slower rupture speed and prolonged rupture duration in the up-dip region are probably caused by the low rigidity of the fault material, e.g., subducted sediments (22, 34), and the increase of dynamic pore fluid pressure (5, 23). For the 2010 Maule and 2005 Sumatra earthquakes,

stable region (with high fluid pressure) at a depth of about 30–45 km in some young subduction zones (e.g., the Nankai trough and Cascadia), with frequent occurrence of episodic tremor and slip (ETS) and LF earthquakes (39). However, for the source region of the Tohoku, Maule, and the 2005 and 2004 Sumatra earthquakes, ETS has not been reported (39).

Materials and Methods

CS (24–27) recovers sparsely distributed sources using an inverse approach and is an active area of research in signal processing and applied mathematics. In the context of great earthquake rupture, we assume that the seismic energy radiated from the source region at a given frequency and time is spatially sparse in the entire rupture area (24). Seismic radiation within a certain time window during the earthquake is represented by its potential source spectrum $\mathbf{x}(f)$ at a set of M spatial source grid points. The observed spectral data at an array of N stations is $\mathbf{b}(f) = \mathbf{A}(f)\mathbf{x}(f) + \mathbf{n}(f)$. Here, $\mathbf{A}(f)$ is the propagation matrix with its nm th element equal to $\exp(-2\pi f\tau_{nm})$, where τ_{nm} is the travel time from location m to station n . The additive noise $\mathbf{n}(f)$ is zero-mean Gaussian. Note that \mathbf{A} samples all possible source locations, but there are only a few active sources. Thus, $\mathbf{x}(f)$ must be sparse.

CS locates the sparse seismic sources $\mathbf{x}(f)$ by minimizing the L2 norm of the difference between the observed $\mathbf{b}(f)$ and modeled spectral data vector $\mathbf{A}(f)\mathbf{x}(f)$ at frequency f , penalized by the L1 norm of the source spectrum vector $\mathbf{x}(f)$, i.e., the following:

$$\hat{\mathbf{x}}(f) = \arg \min \{ \|\mathbf{b}(f) - \mathbf{A}(f)\mathbf{x}(f)\|_2 + \lambda \|\mathbf{x}(f)\|_1 \}. \quad [1]$$

Here, λ is the damping parameter. The sparse problem (Eq. 1) is efficiently solved using convex optimization (28) (SI Text). The L1 norm on the source vector $\mathbf{x}(f)$ in Eq. 1 enforces the sparsity of the estimated source vector $\hat{\mathbf{x}}(f)$ (25–27), that is, only a few elements in $\hat{\mathbf{x}}(f)$ are nonzero (see *Synthetic Tests* in SI Text). This is different from beamforming approaches, which usually only pick one point with the maximum beam power (29).

For a single source, the conventional linear beamforming (29) is perfect even at low frequencies. However, beamforming may fail for multiple-source problems if the sources are within the Rayleigh resolution cell. CS is superior to the conventional beamforming in resolving two or multiple sources within a Rayleigh resolution cell (25) over a broad frequency band (e.g., 0.06–0.6 Hz) (Figs. S3–S6). Superresolution beamforming, e.g., MUSIC (30, 31), can also resolve multiple sources. However, these methods work best for stationary signals and require many observations to obtain a good cross-spectral density matrix estimate, which is rarely the case for transient earthquake signals. MUSIC also needs to estimate the noise subspace, which is difficult in practice. Although superior to linear beamforming, CS and superresolution methods cannot resolve sources too close or with too low frequencies. CS (24) directly works on signals in the frequency domain for

a single observation (time window) without knowing the number of sources and estimating the noise subspace, thus providing a more direct estimation of source parameters. CS is more reliable for multiple-source localization problems and provides a self-consistent and uniform way to study seismic energy radiation from the source region over a wide frequency range, e.g., the Tohoku earthquake (24).

We use dense seismic array data from the United States to analyze the 2011 Tohoku and 2010 Maule earthquakes and data from the Japanese Hi-net array to study the 2004 and 2005 Sumatra earthquakes (Figs. S1 and S2). A sliding window approach (24) is used to obtain $\hat{\mathbf{x}}(f)$, giving the spatial distribution and power of sparse sources at each frequency (frequency band, 0.06–0.6 Hz) and time window (10 or 20 s long). Please see the SI Text for details on data processing, model parameterization, and inversion procedures. To remove unreliable sources, only sources with amplitudes above 0.1 times the maximum element in $\hat{\mathbf{x}}(f)$ are retained for each frequency and time window.

We define $P_{ij}(\theta, f)$ as the power of the j th retained source (at location θ and frequency f) from the inversion in the i th time window. By combining all of the retained sources P_{ij} from all snapshots (time windows), we obtain detailed spatiotemporal variations in seismic radiation during the earthquake at that frequency (e.g., Figs. 2 B–D and F–H, and 3 B–D and F–H). Then we sum over the radiated power with Gaussian smoothing for all of the retained sparse sources at each frequency in all time windows to obtain the along-dip average radiated power with respect to the distance to the plate boundary (Fig. 4) as follows:

$$P(d, f) = \sum_i \sum_j \exp \left\{ -[d_{ij}(\theta, f) - d]^2 / L^2 \right\} P_{ij}(\theta, f), \quad [2]$$

where d is the given distance to the plate boundary (approximately the trench location), $L = 35$ km is the Gaussian smoothing distance, and $d_{ij}(\theta, f)$ is the distance to the plate boundary of the j th retained source (at location θ and frequency f) in the i th time window. The along-dip average radiated power over a frequency band (Fig. 5) can be obtained by summing the average power at various frequencies (Fig. 4) within that band.

ACKNOWLEDGMENTS. We thank the editor and two anonymous reviewers for constructive comments that helped to improve the manuscript. All waveform data were downloaded from the Japanese Hi-net Data Center (with help from Dr. Takahiko Uchide) and from the Incorporated Research Institutions of Seismology. The Generic Mapping Tools (GMT) program by Wessel and Smith was used to plot some of the figures. This research is supported by the Green Scholarship from the Institute of Geophysics and Planetary Physics/Scripps Institution of Oceanography/University of California at San Diego and National Natural Science Foundation of China Grant 41222028 (to H.Y.), and National Science Foundation Grants EAR-1111111, EAR-0944109, and OCE-1030022. This research is also supported by the Chinese Academy of Sciences/State Administration of Foreign Experts Affairs International Partnership Program for Creative Research Teams.

- Kanamori H (1986) Rupture process of subduction-zone earthquakes. *Annu Rev Earth Planet Sci* 14:293–322.
- Heuret A, Lallemand S, Funicello F, Piromallo C, Faccenna C (2011) Physical characteristics of subduction interface type seismogenic zones revisited. *Geochim Geophys Geosyst* 12(1):Q01004, 10.1029/2010GC003230.
- Stern RJ (2002) Subduction zones. *Rev Geophys* 40(4):1012, 10.1029/2001RG000108.
- Lay T, et al. (2012) Depth-varying rupture properties of subduction zone megathrust faults. *J Geophys Res* 117(B4):B04311, 10.1029/2011JB009133.
- Lay T, Bilek S (2007) *The Seismogenic Zone of Subduction Thrust Faults*, eds Dixon TH, Moore JC (Columbia Univ Press, New York), pp 476–511.
- Ammon CJ, et al. (2005) Rupture process of the 2004 Sumatra-Andaman earthquake. *Science* 308(5725):1133–1139, 10.1126/science.1112260.
- Konca AO, et al. (2007) Rupture kinematics of the 2005 Mw 8.6 Nias-Simeulue earthquake from the joint inversion of seismic and geodetic data. *Bull Seismol Soc Am* 97(1A):S307–S322, 10.1785/0120050632.
- Delouis B, Nocquet J-M, Vallée M (2010) Slip distribution of the February 27, 2010 Mw = 8.8 Maule earthquake, central Chile from static and high-rate GPS, InSAR, and broadband teleseismic data. *Geophys Res Lett* 37(17):L17305, 10.1029/2010GL043899.
- Ozawa S, et al. (2011) Coseismic and postseismic slip of the 2011 magnitude-9 Tohoku-Oki earthquake. *Nature* 475(7356):373–376, 10.1038/nature10227.
- Simons M, et al. (2011) The 2011 magnitude 9.0 Tohoku-Oki earthquake: Mosaicking the megathrust from seconds to centuries. *Science* 332(6036):1421–1425.
- Ishii M, Shearer PM, Houston H, Vidale JE (2005) Extent, duration and speed of the 2004 Sumatra-Andaman earthquake imaged by the Hi-Net array. *Nature* 435(7044):933–936.
- Walker KT, Ishii M, Shearer PM (2005) Rupture details of the 28 March 2005 Sumatra Mw 8.6 earthquake imaged with teleseismic P waves. *Geophys Res Lett* 32(24):L24303, 10.1029/2005GL024395.
- Kiser E, Ishii M (2011) The 2010 Mw 8.8 Chile earthquake: Triggering on multiple segments and frequency-dependent rupture behavior. *Geophys Res Lett* 38(7):L07301, 10.1029/2011GL047140.
- Kiser E, Ishii M (2012) The March 11, 2011 Tohoku-oki earthquake and cascading failure of the plate interface. *Geophys Res Lett* 39(7):L00G25, 10.1029/2012GL051170.
- Koper KD, Hutko AR, Lay T, Ammon CJ, Kanamori H (2011) Frequency-dependent rupture process of the 2011 Mw 9.0 Tohoku Earthquake: Comparison of short-period P wave backprojection images and broadband seismic rupture models. *Earth Planets Space* 63(7):599–602, 10.5047/eps.2011.05.026.
- Koper KD, Hutko AR, Lay T (2011) Along-dip variation of teleseismic short-period radiation from the 11 March 2011 Tohoku earthquake (Mw 9.0). *Geophys Res Lett* 38(21):L21309, 10.1029/2011GL049689.
- Wang D, Mori J (2011) Frequency-dependent energy radiation and fault coupling for the 2010 Mw8.8 Maule, Chile, and 2011 Mw9.0 Tohoku, Japan, earthquakes. *Geophys Res Lett* 38(21):L22308, 10.1029/2011GL049652.
- Yao H, Shearer PM, Gerstoft P (2012) Subevents location and rupture imaging using iterative backprojection for the 2011 Tohoku Mw 9.0 earthquake. *Geophys J Int* 190(2):1152–1168.
- Koper KD, Hutko AR, Lay T, Sufri O (2012) Imaging short period seismic radiation from the 27 February 2010 Chile (Mw 8.8) earthquake by backprojection of P, PP, and PKIKP waves. *J Geophys Res* 117(B2):B02308, 10.1029/2011JB008576.
- Scholz CH (1998) Earthquakes and friction laws. *Nature* 391(6662):37–42, 10.1038/34097.
- Bilek SL, Lay T (2002) Tsunami earthquakes possibly widespread manifestations of frictional conditional stability. *Geophys Res Lett* 29(14):1673, 10.1029/2002GL015215.
- Kanamori H, Kikuchi M (1993) The 1992 Nicaragua earthquake: A low tsunami earthquake associated with subducted sediments. *Nature* 361(6414):714–716.
- Ma S (2012) A self-consistent mechanism for slow dynamic deformation and tsunami generation for earthquakes in the shallow subduction zone. *Geophys Res Lett* 39(11):L11310, 10.1029/2012GL051854.

24. Yao H, Gerstoft P, Shearer PM, Meckenbräuker C (2011) Compressive sensing of the Tohoku-Oki Mw 9.0 earthquake: Frequency-dependent rupture modes. *Geophys Res Lett* 38(20):L20310, 10.1029/2011GL049223.
25. Malioutov DM, Mújdac C, Willsky AS (2005) A sparse signal reconstruction perspective for source localization with sensor arrays. *IEEE Trans Signal Process* 53(8):3010–3022, 10.1109/TSP.2005.850882.
26. Candès EJ, Romberg J, Tao T (2006) Robust uncertainty principles: Exact signal reconstruction from highly incomplete frequency information. *IEEE Trans Inf Theory* 52(4):489–509.
27. Donoho D (2006) Compressed sensing. *IEEE Trans Inf Theory* 52(4):1289–1306.
28. Boyd SP, Vandenberghe L (2004) *Convex Optimization* (Cambridge Univ Press, Cambridge, UK).
29. Gerstoft P, Fehrer MC, Sabra KG (2006) When Katrina hit California. *Geophys Res Lett* 33(17):L17308, 10.1029/2006GL027270.
30. Goldstein P, Archuleta RJ (1987) Array analysis of seismic signals. *Geophys Res Lett* 14(1):13–16.
31. Meng L, Inbal A, Ampuero J-P (2011) A window into the complexity of the dynamic rupture of the 2011 Mw 9 Tohoku-Oki earthquake. *Geophys Res Lett* 38(7):L00G07, 10.1029/2011GL048118.
32. Chu RS, et al. (2011) Initiation of the great Mw=9.0 Tohoku-Oki earthquake. *Earth Planet Sci Lett* 308(3–4):277–283, 10.1016/j.epsl.2011.06.03.
33. Wei S, Graves R, Helmberger D, Avouac J-P, Jiang J (2012) Sources of shaking and flooding during the Tohoku-Oki earthquake: A mixture of rupture styles. *Earth Planet Sci Lett* 333–334:91–100, 10.1016/j.epsl.2012.04.006.
34. Ruff LJ (1989) Do trench sediments affect great earthquake occurrence in subduction zones? *Pure Appl Geophys* 129(1–2):263–282.
35. Marone C, Saffer DM (2007) *The Seismogenic Zone of Subduction Thrust Faults*, eds Dixon TH, Moore JC (Columbia Univ Press, New York), pp 346–369.
36. Mitsui Y, Kato N, Fukahata Y, Hirahara K (2012) Megaquake cycle at the Tohoku subduction zone with thermal fluid pressurization near the surface. *Earth Planet Sci Lett* 325–326:21–26, 10.1016/j.epsl.2012.01.026.
37. Rice JR (2006) Heating and weakening of faults during earthquake slip. *J Geophys Res* 111(B5):B05311, 10.1029/2005JB004006.
38. Wibberley CAJ, Shimamoto T (2005) Earthquake slip weakening and asperities explained by thermal pressurization. *Nature* 436(7051):689–692, 10.1038/nature03901.
39. Beroza GC, Ide S (2011) Slow earthquakes and nonvolcanic tremor. *Annu Rev Earth Planet Sci* 39:271–296, 10.1146/annurev-earth-040809-152531.

Supporting Information

Yao et al. 10.1073/pnas.1212790110

SI Text

Data Analysis. The waveform data (downsampled to 10 Hz) for the four earthquakes recorded by the USArray or Hi-net stations (Fig. S1) are 0.05- to 4-Hz bandpass filtered, and the instrument responses are removed. We only use waveforms with P-wave signal-to-noise ratios above 20. Next, we align the waveforms using the first 8 s of the P waves using a cross-correlation method (1). Only waveforms with cross-correlation coefficients above 0.6 with respect to their reference stack are retained for further analysis (Fig. S2).

For the Tohoku, Maule, and 2005 Sumatra earthquakes, we divide the rupture region into 10×10 km source grids, but use 20×20 km grids for the 2004 Sumatra earthquake because this earthquake has a much larger rupture area (2). The equation systems (Eq. 1) to be minimized are large and underdetermined, e.g., for the Tohoku earthquake we have 402 stations and $41 \times 41 = 1,681$ potential source points, giving a complex-valued equation system with 1,681 unknowns and 402 observations. To solve Eq. 1, we use the CVX package (4). A sliding window approach (5) is used to obtain the spectral data (complex variable) in each time window and at each frequency. Within the frequency band of 0.2–0.6 Hz, we use a 10-s time window, and for 0.06–0.2 Hz, a 20-s window, both sliding in steps of 2 s for the Tohoku, Maule, and 2005 Sumatra earthquakes. However, for the 2004 Sumatra earthquake, a 20-s time window sliding in 5-s steps is used for the entire 0.06- to 0.6-Hz band, considering its ~ 600 -s-long rupture time (2, 6). We Fourier transform the waveform data to obtain spectra in each time window, using 128 data points for the 10-s window giving a frequency spacing of 0.08 Hz. For the 20-s window, we use 256 data points giving a frequency spacing of 0.04 Hz. The damping parameter λ in Eq. 1 is set to $0.25\sqrt{N}$, where N is the number of stations (5) for all earthquakes after careful resolution tests using synthetic data. For the detailed setup of CS, we refer to ref. 5.

Synthetic Tests. We perform synthetic tests to assess the resolution and reliability of the compressive-sensing (CS) method at various frequencies and compare it with results from the conventional beamforming method (7). For single-source problems, CS and conventional beamforming generally can identify the model source location equally well. However, CS has much better resolution than conventional beamforming in synthetic tests with two (Figs. S3 and S4) or three sources (Fig. S5).

In the two-source synthetic tests (Fig. S3), we generate synthetic spectral data (with 5% random Gaussian noise added) for the stations in the United States (Fig. S1, *Upper Left*) due to two synthetic sources in the region of the Tohoku earthquake. For all

of the synthetic tests, the input sources are exactly located on the grid points where we invert for source spectra from CS. At 0.55 Hz, CS recovers the input two sources very well and there are two nearby sources (with amplitudes of 0.9 and 0.05) together representing the input source 1. Beamforming resolves these two sources quite well at 0.55 Hz for this source geometry. However, when two sources are set along the direction to the seismic array (Fig. S1, *Upper Left*), beamforming only shows one peak due to interference of the two sources but CS resolves the two input sources very well (Fig. S4). At 0.20 Hz, CS gives two source patches, each with two nearby sources (Fig. S3). The two largest sources are at the correct input source locations. The recovered source patches closely match the input two single sources. At 0.08 Hz, CS also recovers two patches of sources with locations only slightly off (about 10–30 km) the true locations (Fig. S3). The recovered source patch near the input source location 2 consists of three nearby sources. However, at lower frequencies (e.g., 0.20 Hz and 0.08 in Fig. S3), beamforming clearly fails to resolve the input sources, and only shows one peak between the two sources due to severe source spectral interference. These synthetic tests show that CS resolves two sources better than conventional beamforming in the 0.06- to 0.6-Hz frequency band of our analysis (Figs. S3 and S4).

In the three-source synthetic tests (Fig. S5), beamforming clearly fails to recover the source locations at both 0.55 and 0.2 Hz. However, CS recovers three source patches at or near the input source locations at 0.55 and 0.2 Hz. Similar to beamforming, CS cannot resolve the three sources at low frequencies, e.g., at 0.08 Hz, which reflects the resolution limit of CS at low frequencies for multiple sources. Nevertheless, CS is superior to beamforming in resolving multiple sources in the frequency band studied (0.06–0.6 Hz).

Real Data Examples. In our analyses of real data, we have found cases in which the CS and beamforming results largely agree, but also instances where they give different results. In Fig. S6, we show comparisons between CS and beamforming results at 0.2 Hz using the real data for two time windows of the 2010 Maule earthquake. Using the time window of 46–56 s, the CS and beamforming results (Fig. S6, lower row) seem to find very similar source locations. However, using the time window of 39–49 s, the CS and beamforming results (Fig. S6, upper row) are different: beamforming merges the two source patches as seen in the CS results (between latitude 34°S and 36°S) into one patch. Because the true source locations for the real data are unknown, it is not easy to assess differences between CS and beamforming, but our synthetic tests show that the CS results are generally more reliable.

1. Yao H, Shearer PM, Gerstoft P (2012) Subevents location and rupture imaging using iterative backprojection for the 2011 Tohoku Mw 9.0 earthquake. *Geophys J Int* 190(2): 1152–1168.
2. Ammon CJ, et al. (2005) Rupture process of the 2004 Sumatra-Andaman earthquake. *Science* 308(5725):1133–1139, 10.1126/science.1112260.
3. Chu RS, et al. (2011) Initiation of the great Mw=9.0 Tohoku-Oki earthquake. *Earth Planet Sci Lett* 308(3–4):277–283.
4. Grant M, Boyd SP (2011) CVX: Matlab software for disciplined convex programming, version 1.21. Available at <http://cvxr.com/cvx>. Accessed January 25, 2011.

5. Yao H, Gerstoft P, Shearer PM, Mecklenbräuker C (2011) Compressive sensing of the Tohoku-Oki Mw 9.0 earthquake: Frequency-dependent rupture modes. *Geophys Res Lett* 38(20):L20310, 10.1029/2011GL049223.
6. Ishii M, Shearer PM, Houston H, Vidale JE (2005) Extent, duration and speed of the 2004 Sumatra-Andaman earthquake imaged by the Hi-Net array. *Nature* 435(7044): 933–936.
7. Gerstoft P, Fehler MC, Sabra KG (2006) When Katrina hit California. *Geophys Res Lett* 33(17):L17308.

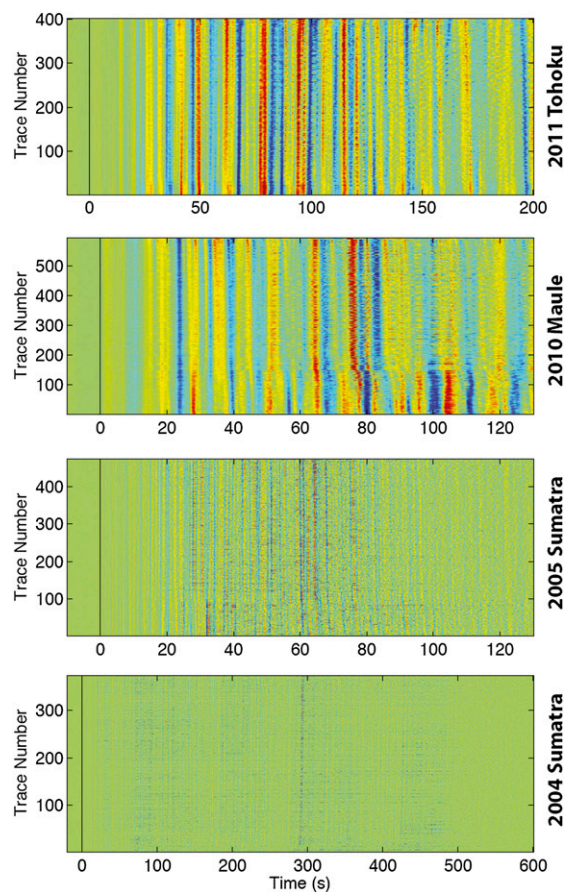


Fig. S2. The aligned waveforms (in the frequency band of 0.05–4 Hz) with good quality used for the CS analysis of each earthquake. The waveforms recorded by the Hi-net stations for the 2004 and 2005 Sumatra earthquakes appear to be dominated by higher frequency energy than the waveforms recorded by the stations in the United States for the Tohoku and Maule earthquakes. This is mainly because the Hi-net stations use short-period high-sensitivity seismographs that suppress energy less than 1 Hz. However, the stations used in the US are all equipped with broadband seismographs.

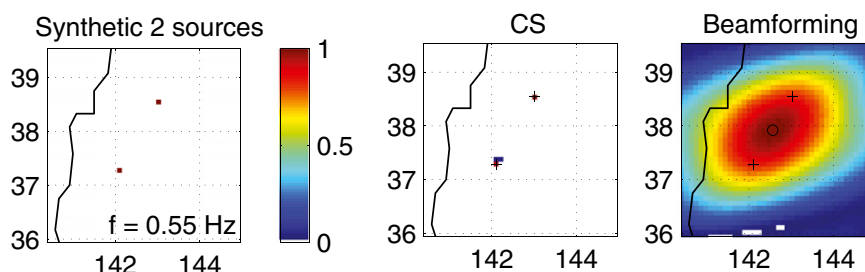
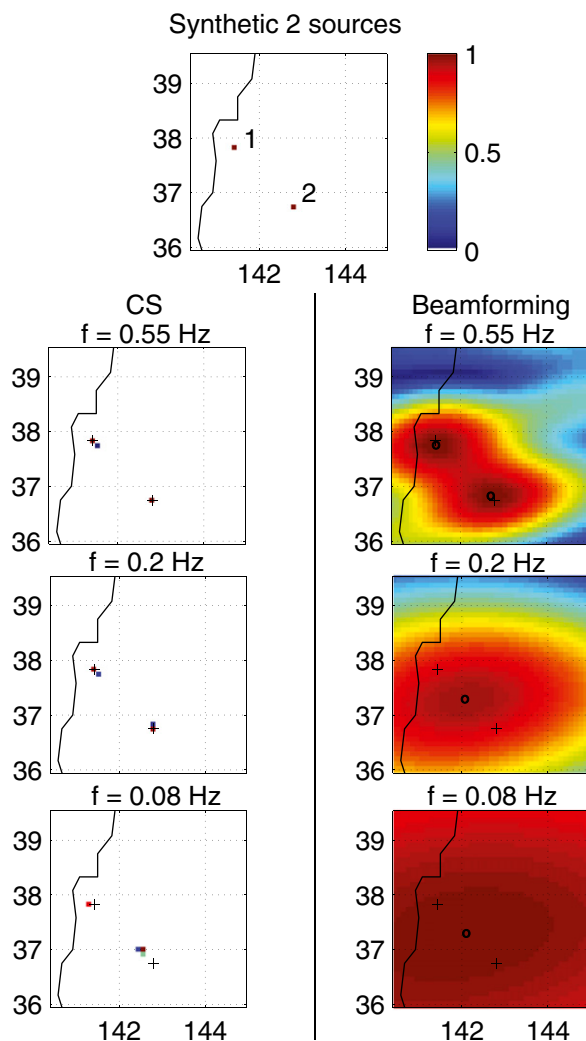


Figure 10 displays four panels showing the evolution of a wave packet. The top row shows the wave packet at $f = 0.2$ Hz and time = [39 49] s. The bottom row shows the wave packet at $f = 0.2$ Hz and time = [46 56] s. The left column shows the wave packet's position and shape, with a blue line indicating the wave packet's path. The right column shows the corresponding intensity maps, with a color scale from 0 to 100. The wave packet is shown as a blue line with markers, and the intensity maps show the wave packet's evolution over time.

5 of 5